ABSTRACT

**NANOCOMPOSITE THERMITE POWDERS WITH IMPROVED
FLOWABILITY PREPARED BY MECHANICAL MILLING**

by
Ci Huang

Nanocomposite thermite powders are of interest to develop varieties of reactive parts and components. Manufacturing these components requires tailoring properties of the thermite powders such as their particle size distributions, particle shapes, and powder flowability. For example, an improved flowability is desired to use these powders as feedstock in additive manufacturing. Arrested reactive milling (ARM) offers a versatile and practical approach for preparing various nanocomposite thermites with fully dense particles, which will retain their structures and mixedness between reactive components while being stored, handled, and processed. However, ARM products usually have broad particle size distributions, rock-like particle shapes, and poor flowability.

Here, ARM is modified to include an additional milling stage to tune the shapes and flowability of the prepared powders. Experiments are performed with aluminum-rich $Al \cdot Fe_2O_3$ thermites. After the initial nanocomposite thermite is prepared in a planetary mill, it is additionally milled at a reduced rotation rate, replacing milling balls with smaller glass beads, and adding different liquid process control agents. Powders with modified particle shapes and size distributions are obtained, which have substantially improved flowability compared to the initial material. The reactivity of modified powders is proved not diminished compared with initial samples but improved in several cases by filament ignition, electro-static discharge and constant volume explosion tests.

NANOCOMPOSITE THERMITE POWDERS WITH IMPROVED
FLOWABILITY PREPARED BY MECHANICAL MILLING

by
Ci Huang

A Thesis
Submitted to the Faculty of
New Jersey Institute of Technology
in Partial Fulfillment of the Requirements for the Degree of
Master of Science in Chemical Engineering

Otto H. York Department of
Chemical, Biological and Pharmaceutical Engineering

May 2017

Blank Page

APPROVAL PAGE

NANOCOMPOSITE THERMITE POWDERS WITH IMPROVED FLOWABILITY PREPARED BY MECHANICAL MILLING

Ci Huang

_____
Dr. Mirko Schoenitz, Thesis Advisor   Date
Associate Research Professor of Chemical, Biological & Pharmaceutical Engineering, NJIT

_____
Dr. Edward L. Dreizin, Committee Member   Date
Distinguished Professor of Chemical, Biological & Pharmaceutical Engineering, NJIT

_____
Dr. Robert B. Barat, Committee Member   Date
Professor of Chemical, Biological & Pharmaceutical Engineering, NJIT

BIOGRAPHICAL SKETCH

Author: Ci Huang

Degree: Master of Science

Date: May 2017

Undergraduate and Graduate Education:

- Master of Science in Chemical Engineering,
  New Jersey Institute of Technology, Newark, United States, NJ,2017

- Bachelor of Engineering in Applied Chemistry,
  Guangdong University of Technology, Guangzhou, P. R. China, 2015

Major: Chemical Engineering

谨以此论文献给我的父亲黄以勉，我的母亲钟碧菲。

感谢你们一直以来的支持，鼓励和包容。

This thesis is dedicated to my beloved father Yimian Huang, mother Bifei Zhong.

For their support, encouragement and unconditional love.

也谨以此论文献给赵扬。

感谢你在这异国他乡给我的慰藉。

This work is also dedicated to Yang Zhao, a special friend, the strongest support I have in this foreign nation,

and the best thing that ever happened to me.

ACKNOWLEDGMENT

First of all, I would like to express my gratitude to Prof. Mirko Schoenitz, who attracted me by the methods of his teaching and drew my interest into this particular research field. As my instructor, his consistent guidance kept me in the right direction when I'm confused and feeling lost in the research. His professional knowledge, kindness and insightful way of thinking continually inspire me throughout this research progress, and will consistently have influences on me in the future.

Special thanks to Prof. Edward L. Dreizin for granting me the opportunity to conduct this research and to join the NJIT Energetic Materials Group. His guidance and professional suggestions for me during this research are gratefully appreciated.

Also, I want to express my gratitude to Prof. Robert B. Barat for his time as my thesis committee member and his valuable opinions and suggestions that help me improve this thesis.

Additionally, thank Lawrence Livermore National Laboratory for the funding of this research.

Finally, I am very much obliged to my fellow students in this group for their helping and advice. Special thanks to Quang, my partner of this project, and Siva, for kindly sharing the usage of equipment when time is pressing me. I also need to thank my parents for supporting me studying abroad.

TABLE OF CONTENTS

LIST OF TABLES

LIST OF FIGURES

LIST OF FIGURES

(Continued)

CHAPTER 1

INTRODUCTION

Reactive nanocomposite thermite powders have been reported as potential candidates for varieties of applications including propellants, explosives and pyrotechnics. There are many different types of nanocomposite thermites prepared using different techniques. For example, Metastable Intermolecular Composite comprising fuel and oxidizer particles were prepared by wet mixing fuel and oxidizer nanoparticles by sonication and pressing [1-6]. Such method does not require complicated machinary, but normally results in nonuniform mixing quality due to the different morphologies of metal fuel and oxidizer [18]. The mixing operation scale is relatively small; scaling up faces various kinds of problems like poorer mixing quality.

Sol-gel sythesis of thermite by deposition of fuel metal into porous-structured oxidizer gel [7], on the other hand, is an approach different from mechanical mixing. The higher mixing quality compared to mechanical mixing, and mild, easily achievable reaction conditions [7] are appealing for certain applications. Self-assembling nano-energetic composites like assembling fuel nanoparticles around oxidizer matrix by monofunctional polymer [8] is a similar approach. This method creates sequential structures for nanoscale oxidizers, letting the fuel metals like aluminum to orderly attach on the structures, which yields highly uniform mixing of metals and metallic oxide. Thus, materials with improved reactivity are accessible this way. However, it is worth noting that only a considerately small amout of materials were reported suitable for Sol-gel sythesis. While the overly complicated preparation protocols of self-assembling materials are hard to achieve.

Moreover, due to the porous morphorlogies, and low bulk density they have in common, these materials have quite limited applications.

Fully dense nanocomposite energetic powders were synthesized from arrested reactive milling (ARM) using vibratory shaker mill [12-16]. Previous studies showed that a large variety of components combinations capable of exothermic reactions was suitable for this method to form reactive materials. By mechanical milling, the starting materials were initialized to a state where the reaction was nearly triggered, at which point the milling was stopped (arrested). The highly reactive thermites were therefore acquired [18]. Unlike thermites prepare by mixing, the oxidizer particles were embeded into the fuel matrix and creating much larger reactive interface area. Although this method can lead to material partially reacted during the process and resulted in a decrease of reactivity, it was found that adjusting the milling conditions can minimize this situation.

Reactivity of nanocomposite thermite powders was studied using various experimental methods, such as constant volume explosion experiment that studies the energy release and combustion rate [12]. Heated filament ignition was applied for material sensitivity measurement and ignition temperature determination [20]. Thermal kinetic analysis was extensively used for low-heating rate kinetic and oxidation study [19, 20]. Combustion shock tube was used to simulate actual explosions [21]. Burn tube experiments were employed to study the propagation of thermite reactions [22-24].

Nanocomposite powders with improved flowability are desirable in ordnance applications, especially in reactive structure manufacturing as the feedstock, where such material can form an explosive charge casing to be triggered after charge detonation or upon impact with the target, creating considerably higher damage power or more desirable

2

effect [14]. This kind of applications normally takes usage of powder bed printing [17] using thermites and other material to fabricate a casing shell that stays inert and maintains structure strength while storage, handling and launching, and exhibits strong combustion performance or other properties upon the proper trigger. Thus, thermites possessing high flowability can benefit fabrication as they will be easier to control than normal thermites that behave like adhesive poor-flow powders gained by conventional preparations.

While many studies emphasized synthesis and combustion characterization of nanocomposite thermites, little to none studies examines how flowability in nanocomposite thermites can be improved, especially for additive manufacturing. In this paper, metastable nanocomposite $Al \cdot Fe_2O_3$ thermites were prepared using Planetary Milling. Two milling steps were employed in the materials preparation stage; first step is high energy milling using steel balls, the second step is low energy milling using glass beads. The objectives of the study are twofold: (1) develop/synthesize nanocomposite thermites with improved flowability milling in different process control agent (PCA); (2) perform materials characterization of prepared samples using heat filament experiment, combustion volume explosion testing (CVE), thermal kinetic analysis (DSC), scanning electron microscopy (SEM), electrostatic discharge test (ESD) to compare combustion performance of 2 step-milling samples with that of 1 step-milling samples.

CHAPTER 2

EXPERIMENTS DETAILS

2.1 Material Preparation

Composite thermite powders with two compositions were explored: $4Al \cdot Fe_2O_3$ and $8Al \cdot Fe_2O_3$, representing thermites with equivalence ratios of 2 and 4, respectively. Starting materials were aluminum -325 mesh, 99.5% purity by Atlantic Equipment Engineers, and iron (III) oxide -325 mesh, 99.5% purity by Alfa Aesar. Composite materials were prepared in a two-step process. Both milling steps were performed in a Retsch 400 PM planetary mill, using custom-made hardened steel vials with thick walls (17 mm). Details for the first and second milling steps are given in **Table 2.1** and **2.2**, respectively. The sample ID in **Table 2.2** is used further in the thesis and represents the sample composition, and the PCA employed in the second milling step. In the first milling step, 10-mm diameter hardened steel balls provided by Frantz Manufacturing, Sterling Steel Division served as milling media. In the second milling step, the milling balls were removed and replaced with glass beads. The glass beads of 75 - 150 µm and 400 - 600 µm nominal diameters supplied by Fox Industries were used. Preliminary inspection of thermite particle sizes and shapes processed by the 75 - 150 µm glass beads showed a lack of useful changes. In particular, electron microscopy showed that particle shapes did not change and particle size analysis showed effectively unchanged particle size distributions. Efficient changes in both particle sizes and shapes were observed for the samples processed using 400 - 600 µm glass beads. Therefore, these glass beads were used in all subsequent experiments. After the second step

milling, the samples were separated from the glass beads by sifting with 100 mesh (150 µm opening size) sieve.

Chemicals used as process control agents (PCA) included hexane (99.5% purity by Science Company), acetonitrile (99.5% purity by VWR International LLC), and stearic acid (97.0% purity by Sigma-Aldrich).

Table 2.1 Milling Parameters for Preparation of Nanocomposite Thermites (1st step milling)

Material	Per vial load g		Milling balls mass g	PCA(Hexane) mL	Milling time min	RPM
	Al	Fe_2O_3				
$4Al \cdot Fe_2O_3$	11.98	18.02	~90	24	60	350
$8Al \cdot Fe_2O_3$	17.24	12.76				

Table 2.2 Milling Parameters for Preparation of Nanocomposite Thermites (2nd step milling)

Sample ID	PCA type	PCA amount	Per vial load of thermite g	Milling media: glass beads µm	Milling media mass g	Milling time hours	RPM
$4Al \cdot Fe_2O_3$:Hex	Hexane	24 mL					
$4Al \cdot Fe_2O_3$:Acn	Acetonitrile						
$4Al \cdot Fe_2O_3$:Dry	Stearic acid	0.6 g	~30	400 - 600	~90	8	200
$8Al \cdot Fe_2O_3$:Hex	Hexane	24 mL					
$8Al \cdot Fe_2O_3$:Acn	Acetonitrile						
$8Al \cdot Fe_2O_3$:Dry	Stearic acid	0.6 g					

2.2 Material Characterization

Particle size distributions for the prepared powders were measured by Low-angle Laser Light Scattering using a Beckman Coulter LS230 Enhanced Particle Analyzer with a Small Volume Module Plus. The powders were suspended in hexane. Ultrasonic agitation of the sample was used. The measurements of all samples were performed using an Al-Hexane measurement model. A separate measurement was performed for $4Al \cdot Fe_2O_3$:Acn in

ethylene glycol suspension with ultrasonic agitation. Hexane is a non-polar solvent and tends to agglomerate the sample, while ethylene glycol is slightly polar and would cause different sample distribution behavior. The measurement model of this sample was accordingly switched to Al-Ethylene Glycol model.

Images of the prepared powders were taken using an LEO 1530VP Field Emission Scanning Electron Microscope. The powder samples were placed on aluminum SEM stubs using double-sided conductive tape. Excess of the powder particles not adhering to the tape was removed by blowing compressed air over the loaded SEM stubs. The images were taken using backscattered electrons, voltage 10 kV, working distance 8 mm.

2.3 Preliminary Flowability Measurements
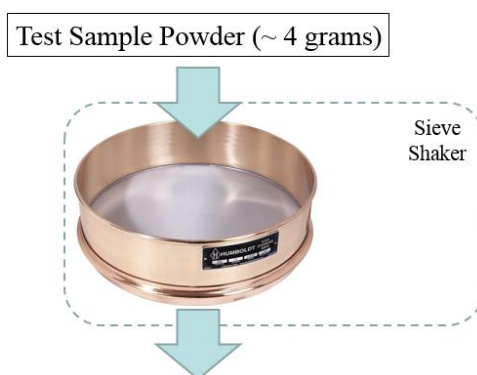
Figure 2.1 Schematic of preliminary flowability measurement

To assess flowability of the prepared powders, and without risking mechanically triggering and igniting a large mass of nanocomposite thermite, a measurement was made involving passing the powder through a shaking sieve, as shown in **Figure 2.1**. The sieve used was 100 mesh (150 µm opening size), which was expected to readily pass all particle sizes in the prepared samples. The sieve was mounted on an Endecotts Octagon 200 test sieve shaker, which was operated with varied amplitude settings and at different durations for

each test. The mass of powder loaded on the sieve was 4 grams. The powder passed through the sieve was collected in a catch pan and weighed using an Acculab Sartorius group balance.

2.4 Ignition and Combustion Experiments

2.4.1 Filament Ignition Experiments
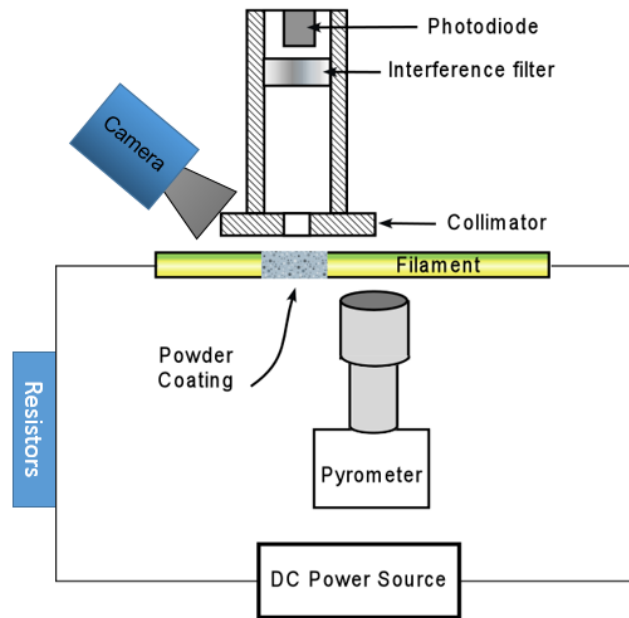
Figure 2.2 Schematic of heated filament ignition experiment.

Ignition of prepared materials was performed in air using an electrically heated filament [25]. These experiments aimed to determine whether the processing changed the ignition temperature of the thermite powders. Experiment configuration is shown in **Figure 2.**2. The test powder was coated on a 0.5-mm diameter 52-mm long nickel-chromium filament. Only an approximately 10-mm length fraction of the filament was coated with the powder. To prepare the coatings, the powders were suspended in hexane. Typically, 10 mg of

powder was placed in 2 mL of hexane. The suspension was deposited on the filament using

a paint brush. The filament was dried prior to the experiment and then heated electrically

using an EXIDE U1SM 12-V battery connected in series with a 0.5-Ohm resistor. The

filament temperature was measured using a high-speed infrared pyrometer OS4001-V1 by

Omega Engineering, focused on an uncoated portion of the filament adjacent to the coating.

It recorded the temperature vs. time curve starting with the filament temperature of 400 °C,

at which the filament became sufficiently luminous. The powder coating was imaged in

real time using Redlake MotionPro 500 video camera. The filament temperature at the

instant of ignition was treated as the ignition temperature. If the powder ignited before the

filament temperature could be measured, i.e., before the filament is sufficiently luminous,

the ignition temperature was identified by linearly extrapolating the measured temperature

vs. time curve to earlier times.

2.4.2 Electrostatic Discharge (ESD) Multilayer Ignition Experiments
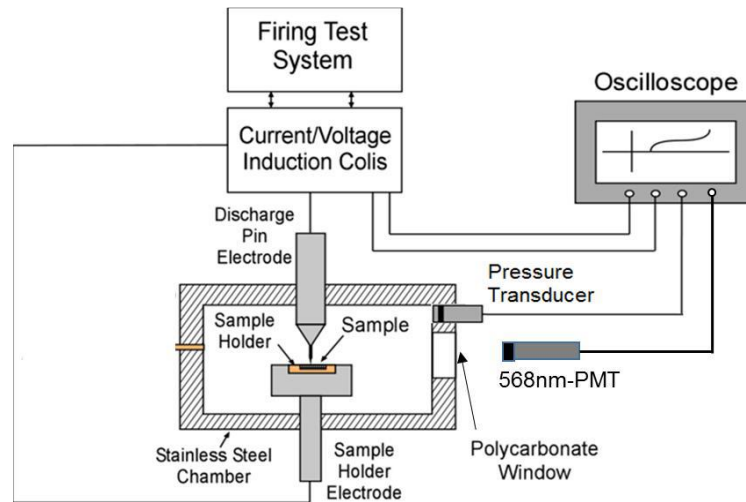
Figure 2.3 Schematic of electrostatic discharge multilayer combustion experiment.

The objective of these experiments was to observe whether processing affected the rate of ignition and combustion of the ESD-ignited powders. The experimental setup was described in detail elsewhere [26] and as shown in **Figure 2.3**. The model 931 firing test system by Electro-Tech Systems, Inc., served as the ESD power source, with the voltage set to 12 kV and was used to charge a 2000 pF capacitor. A high voltage pin-electrode was connected to the positive voltage; the negative voltage was grounded and connected to the sample holder. The capacitor's discharge through the high-voltage-pin-electrode to the composite powder was triggered electronically. A small amount of sample powder filled up a 0.5-mm deep, 6.7-mm diameter cavity in a brass plate. The loaded sample holder was weighed before and after each test; thus, the mass of the material participated in combustion was determined. The measured pressures (see below) were then normalized per mass of the ejected powder. Both electrodes were placed inside a 624 cm^3 sealed test chamber. The spark distance was maintained at approximately 1 mm in all runs. Induction coils by Pearson Electronics were used to monitor the spark current and voltage. A filtered photomultiplier (PMT) equipped with a 568-nm interference filter recorded the optical emission produced by the ignited samples. A PCB piezotronics model 482A21 pressure transducer was mounted in the chamber and measured the pressure generated by the ignited powder in real time. The pressure signal was further processed using a signal conditioner and recorded using a Rigol model DS1054 digital oscilloscope. In addition, emission signals from the PMT were recorded using the same oscilloscope. For each sample powder, at least three ignition runs were conducted.

2.4.3 Monolayer ESD Quenched Particles Capture Experiments

These experiments were aimed to capture and study individually burning particles from the spark ignition, and to describe the structure changes, morphology difference of quenched particles and the spatial distribution as well. The experiment device was the same model 931 firing test system as described in the previous subsection, with the identical voltage setting and using the same capacitor, as shown in **Figure 2.4**. By replacing the original test chamber with an open platform, an aluminum foil coated on a rectangular aluminum plate of 30 mm by length and approximately 5 mm by width was attached to one end of a plastic arm mounted adjacent to the sample holder and the pin-electrode. The arm was free to move around the other end. The configuration of electrodes remains the same as that of multilayer ESD experiment previously described. A small amount of sample powder was applied to a double-sided carbon tape adhered on a brass substrate. The tape was then blown by compressed air to remove excess powder to create a monolayer of sample coating. The spark distance was maintained at approximately 1 mm in all runs. For each sample, at least five ignition runs were conducted. The aluminum foil for each sample was then removed from the arm, and SEM pictures were taken for all sample foils. In each picture, the coordinates were recorded and used to indicate the positions of capture particles. The structures of quenched particles were categorized based on structures, shapes, and scales of phase-separation.
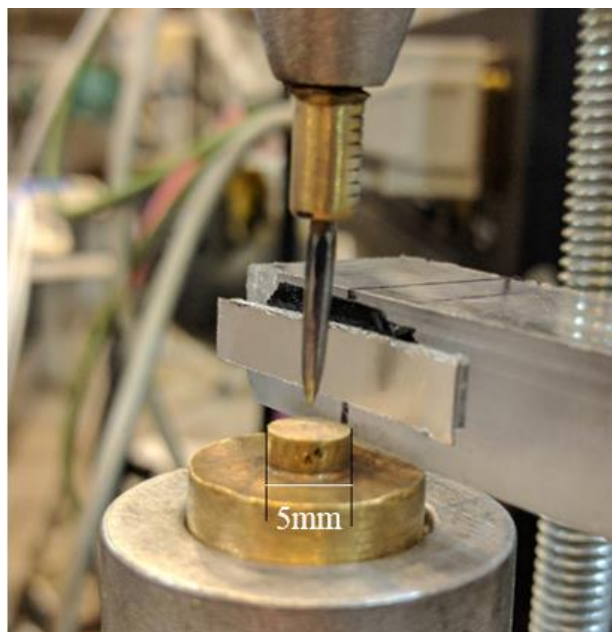
Figure 2.4 Experimental configuration of electrostatic discharge monolayer particles quenched experiment.

2.4.4 Constant Volume Explosion Experiment
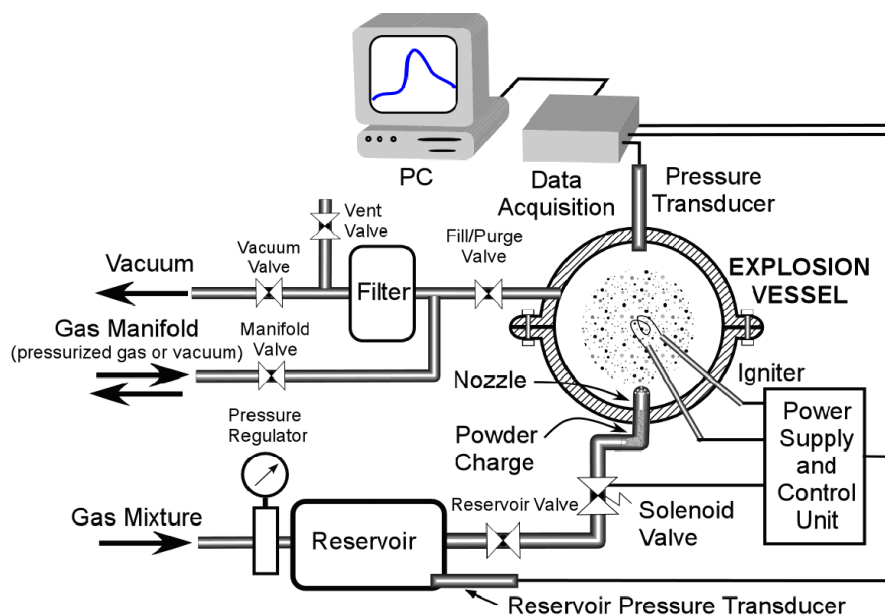
Figure 2.5 Schematic of constant volume explosion experiment.

In these experiments, powders are dispersed by a pressure blast into a chamber, and their combustion characteristics are affected by both the properties of the powders, and by the way they are dispersed. The details of the experiment were described elsewhere [27-29] and

as shown in **Figure 2.5**. Powders that flow better are expected to be more effectively dispersed and aerosolized, leading to a better combustion performance. Conversely, coarser particles are usually causing diminished pressure and rate of pressure rise, serving respectively as indicators of energy release and rate of combustion. The vessel consists of two halves; the top half is removed prior to each experiment. With the vessel opened, 4 g of powder was placed in a pipe elbow under the nozzle. The vessel was closed and evacuated to about one-third of an atmosphere. Air was the only oxidizer used in this project. A reservoir was filled with air to a pressure of 60 psi. The aerosolized powder was introduced into the vessel using an air blast delivered from the reservoir filled with air. The pre-ignition pressure in the vessel was close to 1 atm. After a 0.3-s delay to minimize the turbulence, the powder cloud was ignited by an electrically heated tungsten wire placed at the center of the vessel. The estimated total electrical energy supplied to the igniter was around 30 J. The pressure inside the vessel was recorded as a function of time using a pressure transducer by Schaevitz Sensors. The ratio of maximum pressure to the initial pressure, $p_{\mathrm{max}}/p_{\mathrm{initial}}$, and the maximum rate of pressure rise, $(\mathrm{d}p/\mathrm{d}t)_{\mathrm{max}}$ were obtained to characterize the combustion energy release during the experiment and the rate of combustion, respectively. After the collection of combustion products and cleaning the interior of the vessel, the nozzle was removed and the vessel was again closed and evacuated. A gas blast from the reservoir through the solenoid valve was repeated to clean the pipe elbow and remove residue of the original powder charge that was not dispersed during the combustion experiment.

2.5 Thermal Analysis Experiment

All prepared samples were characterized using differential scanning calorimetry (DSC) in a Netzsch STA409PG thermal analyzer with a 250 µL alumina crucible as the sample holder. The main goal of this experiment is to obtain the reaction kinetics of fully oxidized samples and compare two steps balls and glass beads milled samples to 1 step balls milled samples. The mass of test sample for each measurement run was approximately 4.5 mg. To determine oxidation reactions, samples of interest were heated in ultra-high purity argon (99.999%) at the flowrate of 50 mL/min and at the heating rate of 5, 10 and 20 K/min. Each measurement was programmed to heat the sample to 650 ℃ at a constant heating rate and to hold for 30 minutes to fully react the material. The reacted and thus inert sample then experienced a second heating to 650 ℃ and the heat flow trace of inert second heating was used for baseline subtraction. For each sample, the subtracted heat flow trace (DSC curve) with yielded exothermic peaks was used to calculate the activation energy for each peak and treated as the characterization of reaction kinetics.

CHAPTER 3

RESULTS AND DISCUSSION

SEM images of $4Al \cdot Fe_2O_3$ and $8Al \cdot Fe_2O_3$ composite powders prepared by the first step milling only (conventional nanocomposite thermites prepared by arrested reactive milling) are shown in **Figure 3.1** and **3.2**, respectively. Particles are roughly equiaxial but contain sharp edges. More fine particles are seen for the $4Al \cdot Fe_2O_3$ sample; these particles most likely represent unattached fine Fe_2O_3.
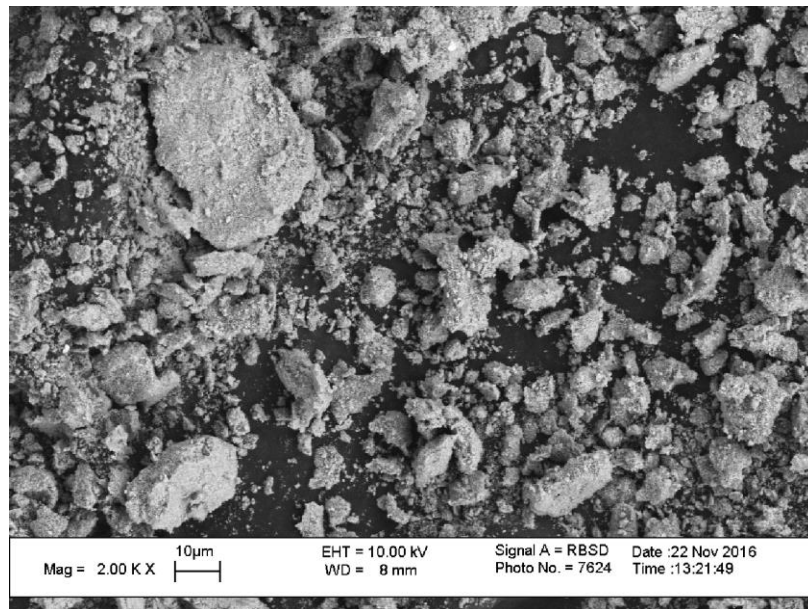
Figure 3.1 $4Al \cdot Fe_2O_3$ nanocomposite thermite prepared by one-step milling.

The unattached Fe_2O_3 particles, as well as composite particle structure, is better seen in the close-up image for the $4Al \cdot Fe_2O_3$ nanocomposite thermite shown at a high magnification in **Figure 3.3** below.
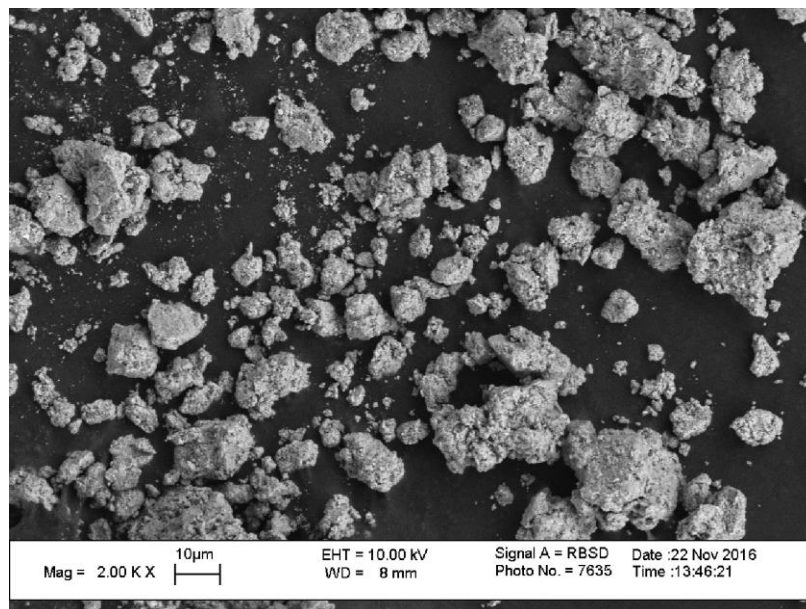
Figure 3.2 8Al·Fe_2O_3 nanocomposite thermite prepared by one-step milling.
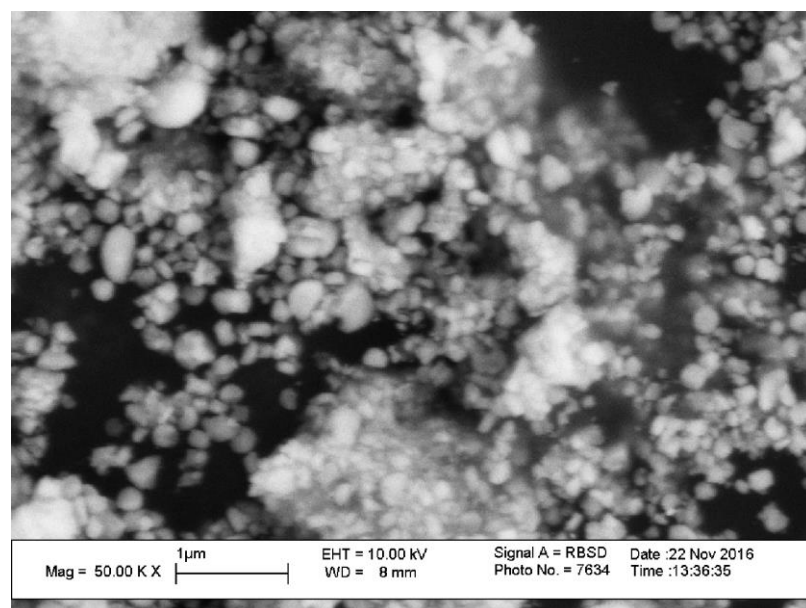
Figure 3.3 A high-magnification image of 4Al·Fe_2O_3 nanocomposite thermite prepared by one-step milling. Fine unattached particles are Fe_2O_3; composite particles, in which Fe_2O_3 particles are embedded in aluminum, are also visible.

Powder morphology changes noticeably after their low-energy milling with glass beads. For 4Al·Fe_2O_3:Hex sample, shown in **Figure 3.4**, many large, ca. 10-µm particles with smooth surfaces are formed. However, the sample still contains many fine particles, for which the shapes remain rock-like rather than rounded.
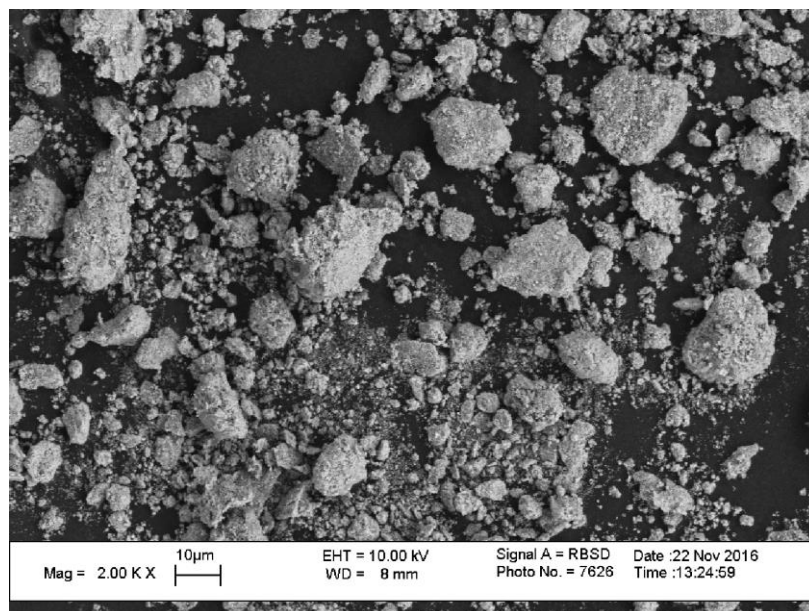
Figure 3.4 4Al·Fe_2O_3:Hex nanocomposite thermite (see **Table 2.2** for details).

The 4Al·Fe_2O_3 sample processed in acetonitrile, a polar solvent, shown in **Figure 3.5**, appears to contain a large amount of very fine particles, some of which coat surface of coarser particles and some are unattached. The coarser particles appear to possess sponge-like porous morphology.
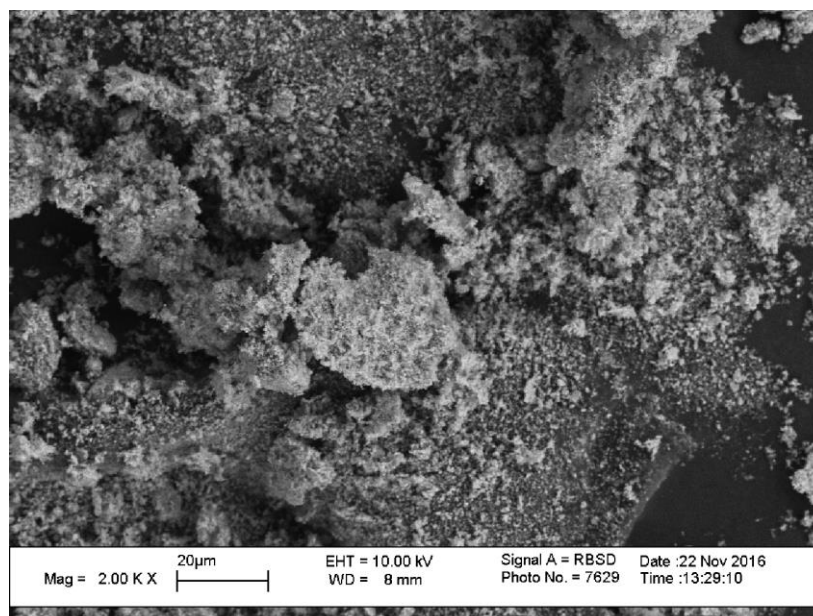
Figure 3.5 4Al·Fe_2O_3:Acn nanocomposite thermite (see **Table 2.2** for details).

The morphology of $4Al \cdot Fe_2O_3$ sample processed in steric acid, shown in **Figure 3.6** is somehow similar to $4Al \cdot Fe_2O_3$:Hex, containing large composite particles and many fine ones.
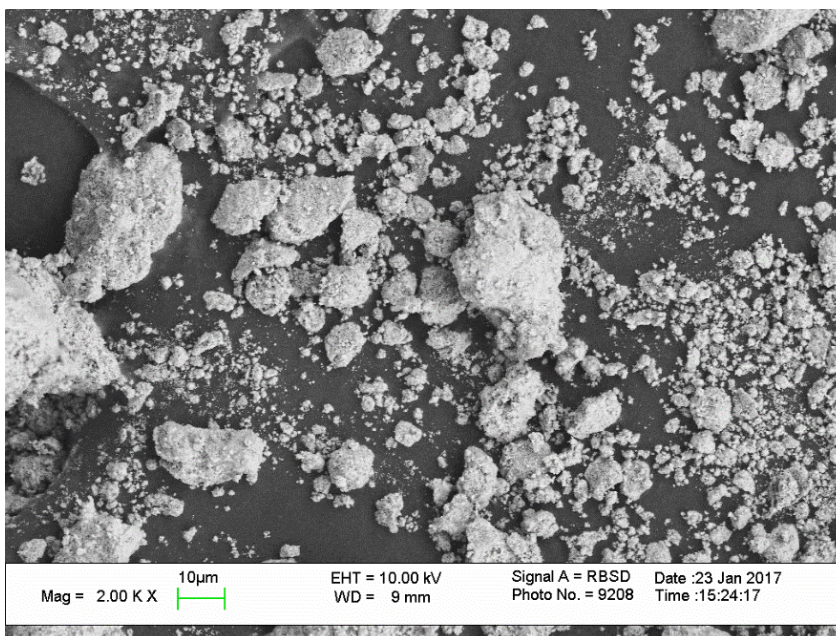
Figure 3.6 $4Al \cdot Fe_2O_3$:Dry nanocomposite thermite (see **Table 2.2** for details).

The particles are observed to be much more rounded in **Figure 3.7** for the $8Al \cdot Fe_2O_3$:Hex sample compared to single stage milling sample. There are no unattached fine particles, which must have been included in the larger particles seen in the SEM image in **Figure 3.7**. The surface is relatively smooth and does not show clear compositional contrast on the scale resolved in the present image.

When $8Al \cdot Fe_2O_3$ powder is processed in acetonitrile, the powder contains larger and most rounded particles. Multiple unattached very fine particles were observed, some of which appear to be covering larger particle surface, as shown in **Figure 3.8**. This morphology, with coarse particles covered with a thin layer of very fine particles, is similar to that targeted by dry coating, a technique aimed to improve flowability of many commercial powders. The fine particles reduce the probability of agglomeration of larger

particles and serve as an effective lubricant when the powder flows. Additionally, the

particle surface roughness appears to be increased after milling with glass beads in

acetonitrile.
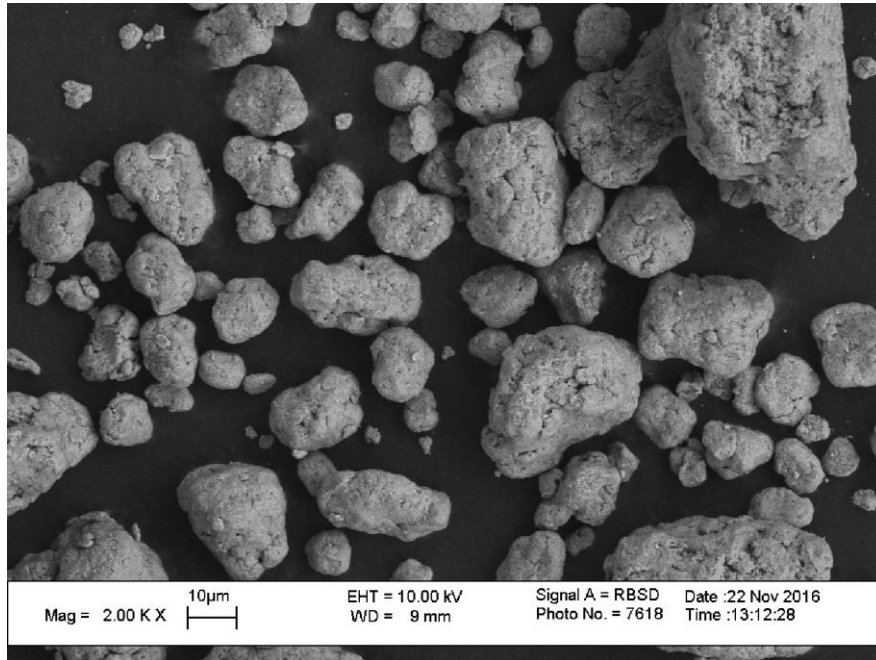
Figure 3.7 $8Al \cdot Fe_2O_3$:Hex nanocomposite thermite (see **Table 2.2** for details).
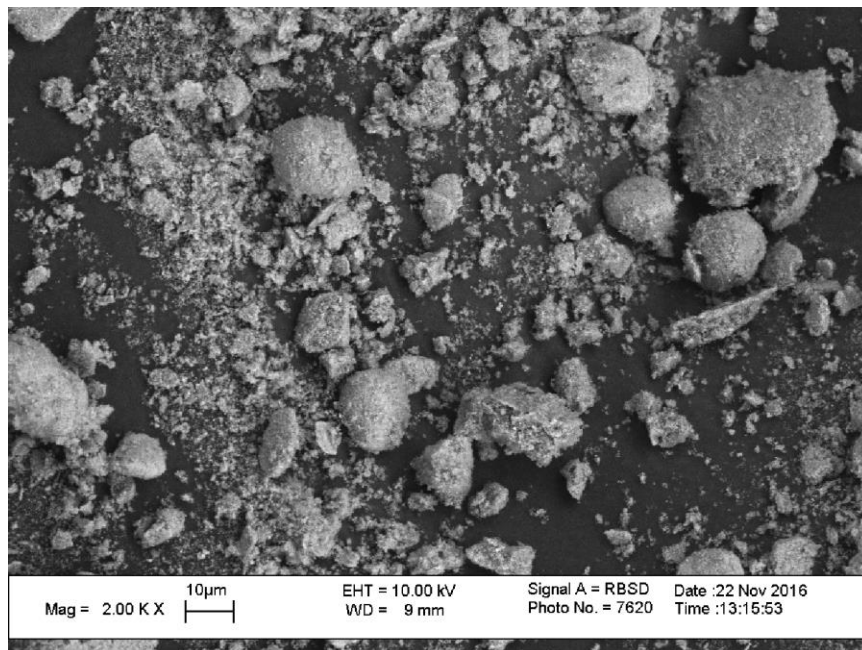
Figure 3.8 $8Al \cdot Fe_2O_3$:Acn nanocomposite thermite (see **Table 2.2** for details).
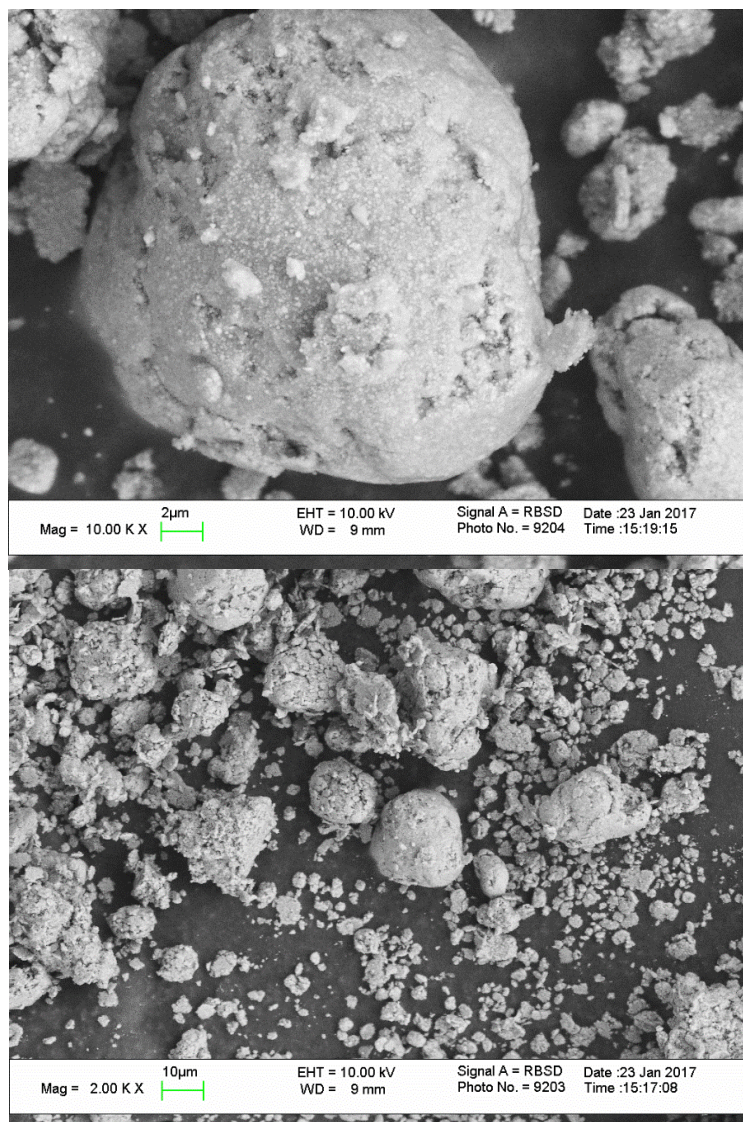
Figure 3.9 8Al·Fe_2O_3:Dry nanocomposite thermite (see **Table 2.2** for details).

Low-energy milling 8Al·Fe_2O_3 processed in steric acid, shown in **Figure 3.9** seems to break up agglomerations and form dense coarse particles with very fine Fe_2O_3 particle coated on the surface. Many large particles with the same size were observed here.

Particle size distributions for different 4Al·Fe_2O_3 powders are shown in **Figure 3.10**. For this material, the range of particle sizes and the average particle size are nearly preserved after low-energy milling in hexane. However, in qualitative agreement with SEM observations, the particle size distribution appears to become more bimodal. The low-

energy milling in acetonitrile clearly causes the formation of large porous agglomerates as seen in the SEM and as was observed to exhibit larger particle size that exceeds the sieve opening size (150 µm) based on the measured particle size distribution in hexane suspension. Thus, an additional measurement for $4Al \cdot Fe_2O_3$:Acn was performed in ethylene glycol suspension using an Al-Ethylene Glycol fluid model (see Section **2.2** for detail). As shown in **Figure 3.10**, a marked reduction of particle size range was observed compared to the measurement done in hexane suspension. This observation suggests that the large aggregates found in SEM (see **Figure 3.**5) and hexane-suspended size measurement was effectively deagglomerated in the additional measurement in ethylene glycol.
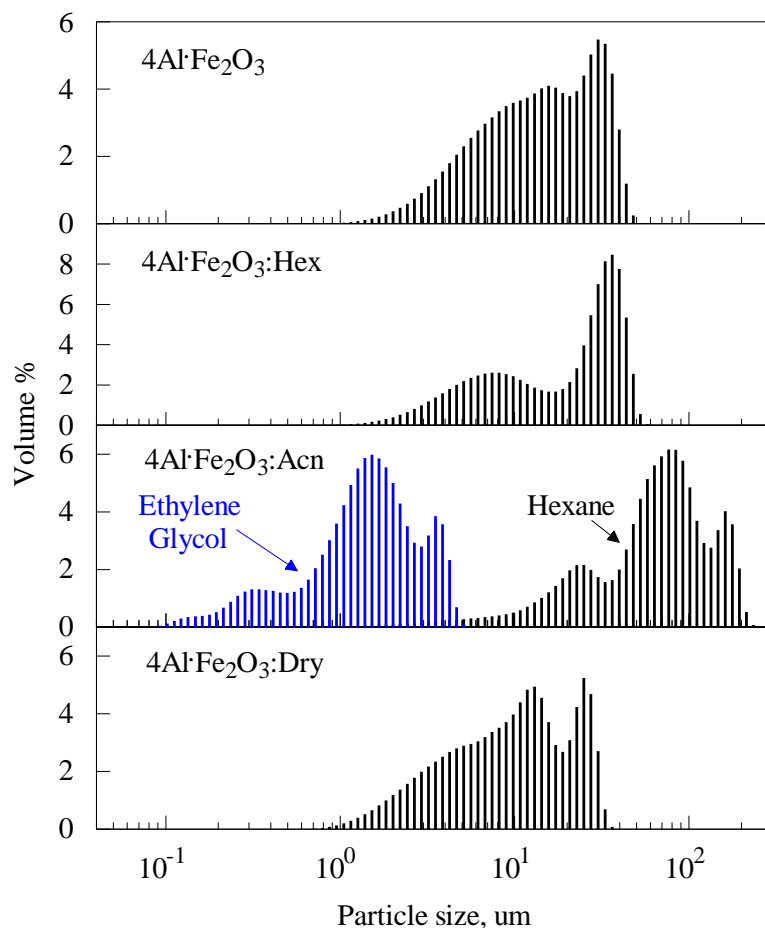
Figure 3.10 Particle size distributions for different $4Al \cdot Fe_2O_3$ nanocomposite thermites.

Particle size distributions for different $8Al \cdot Fe_2O_3$ powders are shown in **Figure 3.11**. Despite a substantial change in the particle morphology caused by its low-energy processing in hexane, the change in the particle size distribution is relatively subtle. The biggest effect is a reduction in the particle size distribution tail extending to fine particle sizes. Conversely, processing in acetonitrile seems to generate finer particles. Dry processing appears to concentrate most of the material in relatively coarse aggregates; however, the entire range of particle sizes is not changed substantially for any of the $8Al \cdot Fe_2O_3$ powders processed by the second milling step.
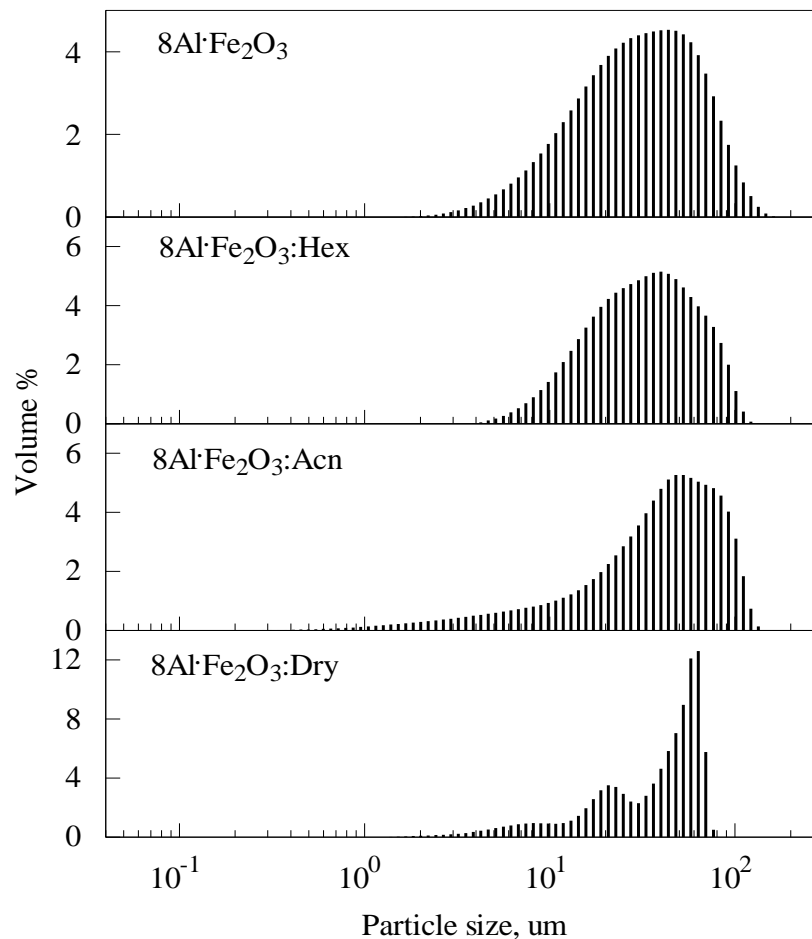
Figure 3.11 Particle size distributions for different $8Al \cdot Fe_2O_3$ nanocomposite thermites.

Results of the sieve shaker experiments aimed to preliminarily quantify flowability of the prepared powders are shown in **Figure 3.12**. The amplitude settings of the shaker

were different, at 3 and 5 for $8Al \cdot Fe_2O_3$ and $4Al \cdot Fe_2O_3$ powders, respectively. These

settings were selected to ensure some powder flow for the samples prepared using a single

step milling. For $8Al \cdot Fe_2O_3$, the measurements could be usefully performed with two time

durations of 50 and 100 s, whereas only one duration of 100 s was used for $4Al \cdot Fe_2O_3$. It

is observed that the flowability for all samples was substantially improved as a result of

the second low-energy milling step. For $8Al \cdot Fe_2O_3$, it appears that powders processed with

all tested PCAs show a similar improvement in flowability. However, for $4Al \cdot Fe_2O_3$, the

effect of PCA is more dramatic, with both acetonitrile and stearic acid producing much

better flowing powders than hexane. This observation is particularly interesting

considering that processing this material in acetonitrile generates a coarser, agglomerated

powder while its processing in stearic acid appears to break up agglomerated particles (see

Figure 3.10). The sole quality shared by all low-energy processed samples is the surface

coating of fine particles that can lubricate the powder and prevent adhesion.
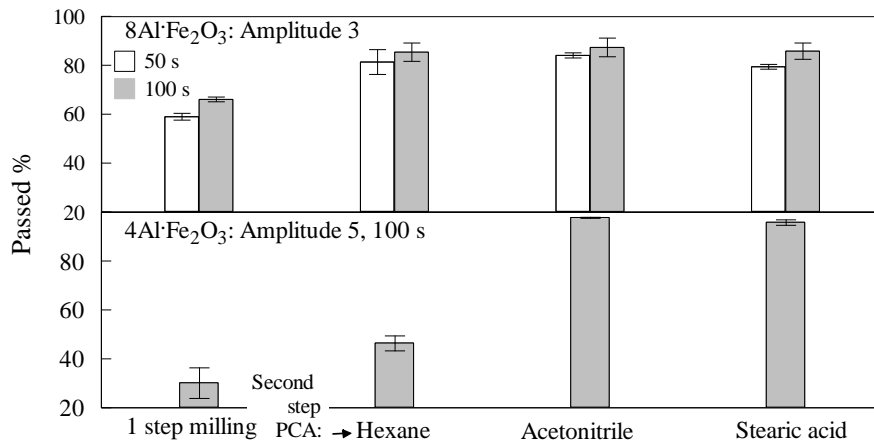
Figure 3.12 Mass fraction of the powder load passed through the sieve during the test for
different nanocomposite thermites.

The sample ignitions of heated filament experiments were recorded by a high-speed

camera as shown in **Figure 3.13**. Two image sequences are shown as representative runs

for each composition of prepared thermites. Both image sequences were taken at the

heating rate of ca. 840 K/s. The frame rate was 500 fps and the exposure time for each frame was 2 ms. The first frame of each image sequence is the instant of ignition.

(a) $4Al \cdot Fe_2O_3$

(b) $8Al \cdot Fe_2O_3$
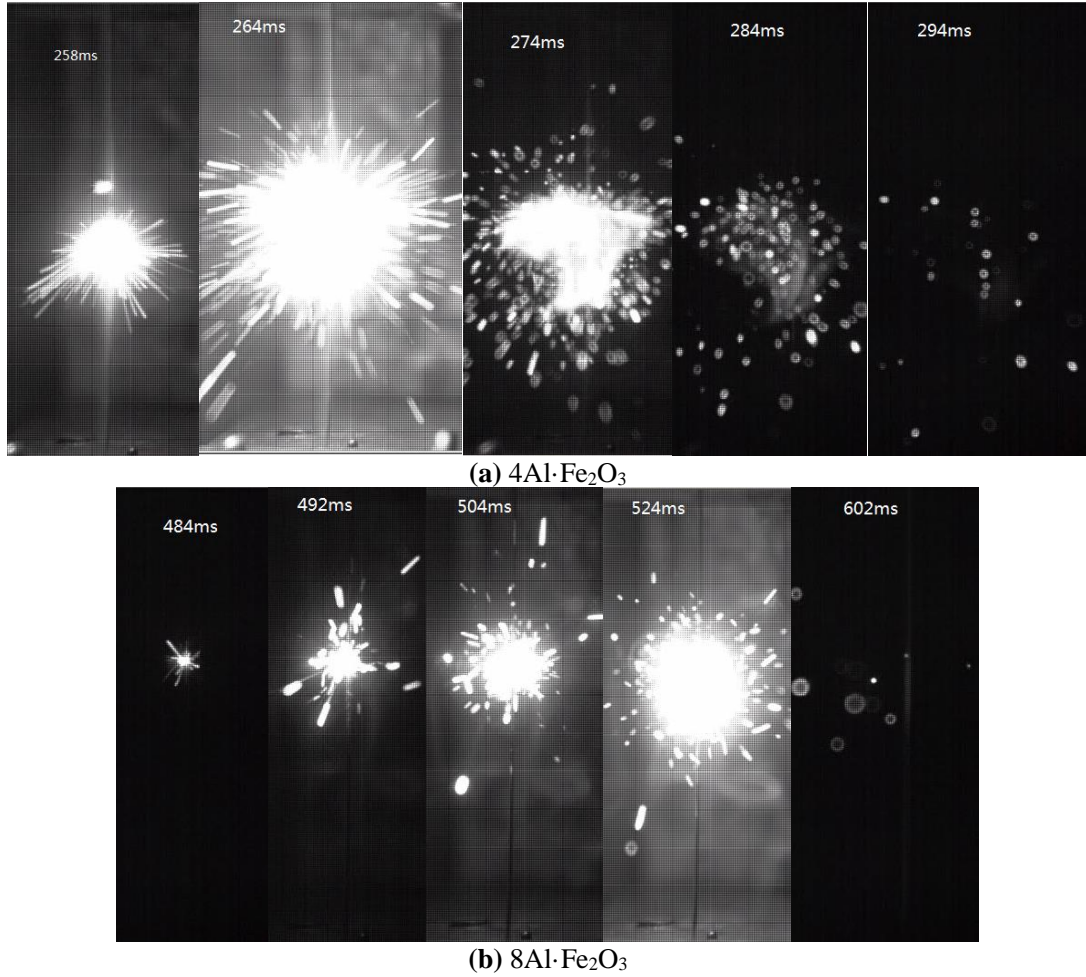
Figure 3.13 Sequences of images captured by high speed camera in filament ignition experiment for samples of different composition.

For both sample compositions, at the instant of ignition, a portion a powder coating became incandescent, and burning particles started to be ejected from the coating on the heated wire. The sample powder of $4Al \cdot Fe_2O_3$ generally burned faster than $8Al \cdot Fe_2O_3$ as they formed a bright burning cloud of the whole powder coating at the instant of ignition, whereas the $8Al \cdot Fe_2O_3$ coatings were ignited gradually from one end to the other. And the samples of $4Al \cdot Fe_2O_3$ were all burned out before the wire started to glow. This observation

was not made for 8Al·Fe$_2$O$_3$ samples as they were mostly not fully reacted until the heated filament was showing some brightness.

Ignition temperatures measured in the heated filament ignition experiments are shown in **Figure 3.14** for different materials. It is observed that the ignition temperatures for both 4Al·Fe$_2$O$_3$ and 8Al·Fe$_2$O$_3$ powders were unaffected by additional low-energy processing except for the case when the processing was performed in acetonitrile. In the latter case, the ignition temperature is reduced compared to other cases, suggesting that acetonitrile chemically alters the surface of the prepared nanocomposite thermite powders.
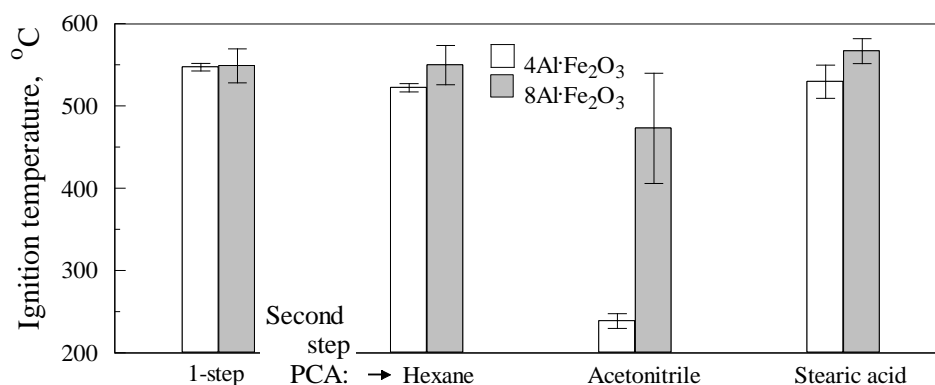
Figure 3.14 Ignition temperatures for different nanocomposite thermite powders measured using a heated filament experiment.

Optical emission traces and characteristic pressure traces measured in the ESD ignition experiments are shown in **Figures 3.15** and **3.16** for 4Al·Fe$_2$O$_3$ and 8Al·Fe$_2$O$_3$, respectively. The emission traces and pressure traces exhibit a well correlating relationship, in which the duration of emission is basically the same as that of pressure increase. In other words, the emission signal represents the on-going reaction of thermite releasing energy and generating pressure. For 4Al·Fe$_2$O$_3$, all emission and pressure traces appear to be qualitatively similar to one another, indicating that additional milling stage did not show much effect on energy release. It is worth noting that the overall optical pulse duration appears to be smaller for 4Al·Fe$_2$O$_3$:Acn sample. For 8Al·Fe$_2$O$_3$, the traces are generally

longer, most likely due to the presence of excess aluminum reacting with surrounding air. However, the traces for $8Al \cdot Fe_2O_3$:Acn and $8Al \cdot Fe_2O_3$:Dry samples are much shorter than the ones for the single stage milled $8Al \cdot Fe_2O_3$ and $8Al \cdot Fe_2O_3$:Hex. The shorter traces of these two samples also generate greater emission intensities (higher PMT voltage) and higher characteristic pressure at short reaction times.

Intriguingly, the sample prepared using low-energy milling in hexane, which forms the most spheroidal particles, exhibits a slightly delayed ignition and accelerated rate of pressure rise compared to the starting nanocomposite thermite prepared by 1-step milling. For powders processed by low-energy milling using acetonitrile and stearic acid, the reaction begins faster and proceeds to much higher pressures than observed for the initial nano-thermite. As in CVE experiment, the outcome of this test depends on both reactivity of the material and on how well the material is dispersed upon interaction with the ESD. It is hypothesized that both $8Al \cdot Fe_2O_3$:Dry and $8Al \cdot Fe_2O_3$:Acn samples are more readily aerosolized and thus burn more efficiently than other powders. In addition, a reduced ignition temperature observed for $8Al \cdot Fe_2O_3$:Acn may be causing a more efficient combustion of that material.
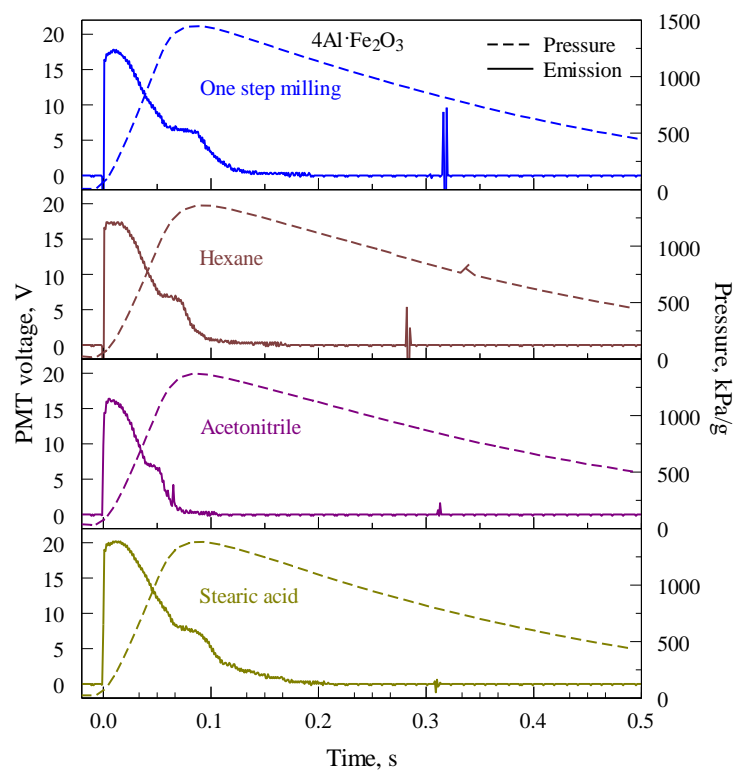
Figure 3.15 Optical emission traces and characteristic pressure traces measured in ESD ignition experiments with different $4Al \cdot Fe_2O_3$ powders.
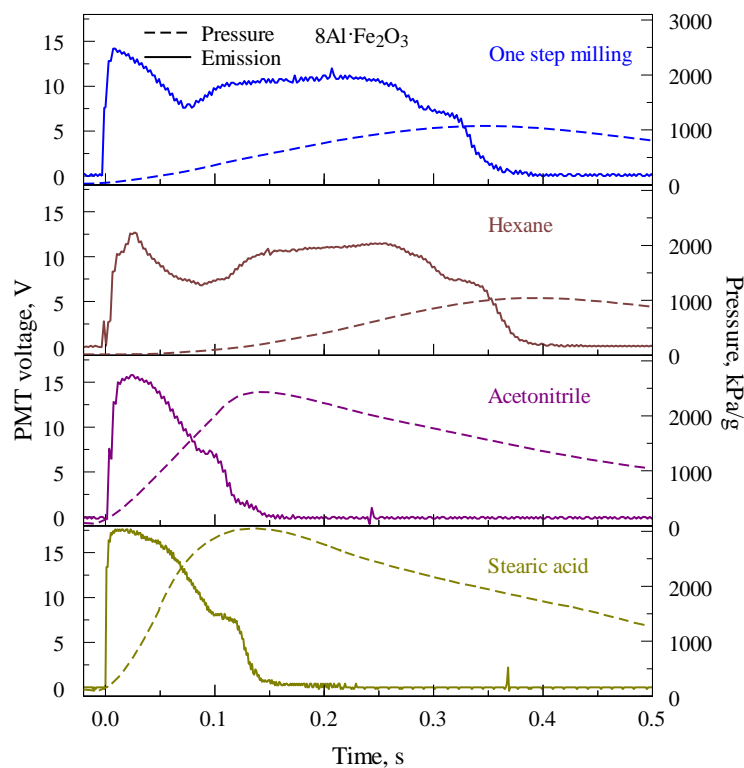
Figure 3.16 Optical emission traces and characteristic pressure traces measured in ESD ignition experiments with different $8Al \cdot Fe_2O_3$ powders.

The trends observed for individual traces shown in **Figure 3.15** and **3.16**are further supported when average values of the measured pressures are considered, as shown in **Figure 3.17**, based on at least five measurements for each material. Low-energy processing with acetonitrile or stearic acid as PCA causes a significant increase in the measured pressure for $8Al \cdot Fe_2O_3$ ignited by ESD.
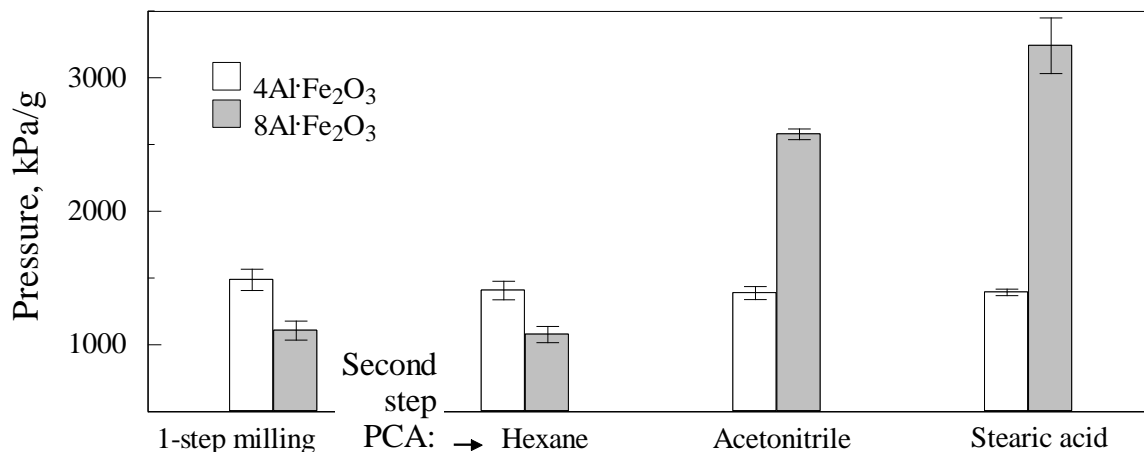
Figure 3.17 Maximum pressures measured in ESD ignition experiments for different $Al \cdot Fe_2O_3$ nanocomposite thermite powders.

Results of initial CVE experiments are illustrated in **Figure 3.18**. For both $4Al \cdot Fe_2O_3$ and $8Al \cdot Fe_2O_3$ thermites, the powders subjected to low-energy second step milling exhibit a higher pressure than the powder milled in one step. This effect is most likely due to a better aerosolization of the 2-step milled powders. For $4Al \cdot Fe_2O_3$, the low-energy processing in acetonitrile yields a material $4Al \cdot Fe_2O_3$:Acn that ignites while being introduced into the vessel with a pressurized gas blast (pressure starts rising rapidly during the initial pressure ramp, representing the introduction of the powder and raising the pressure in the explosion vessel to the initial 1-atm value). This ignition is triggered mechanically and may suggest a substantially increased sensitivity to friction initiation.
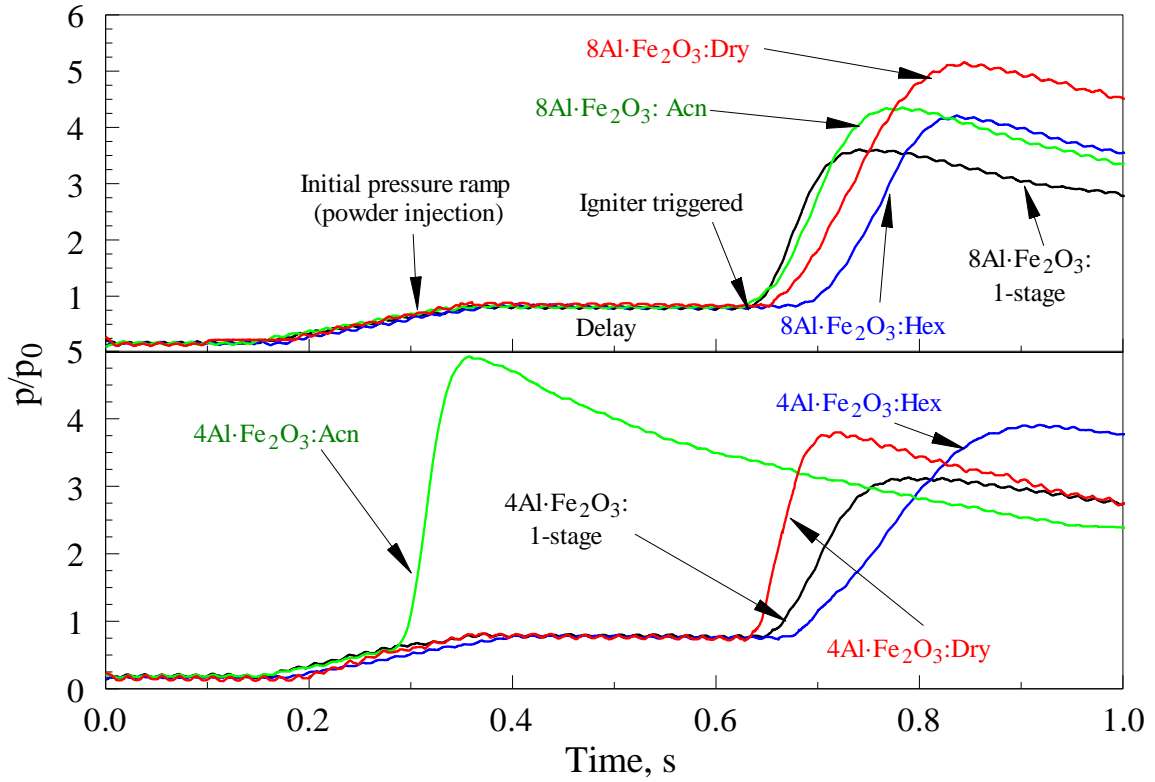
Figure 3.18 Normalized pressure traces measured in CVE experiments with different nanocomposite thermite powders.

The monolayer ESD quenched particle experiment provide a general idea of the reaction regime of individual burning particle. The schematic diagram of the axial-symmetric spatial distribution of thermite captured on aluminum foil is shown in **Figure 3.19**.
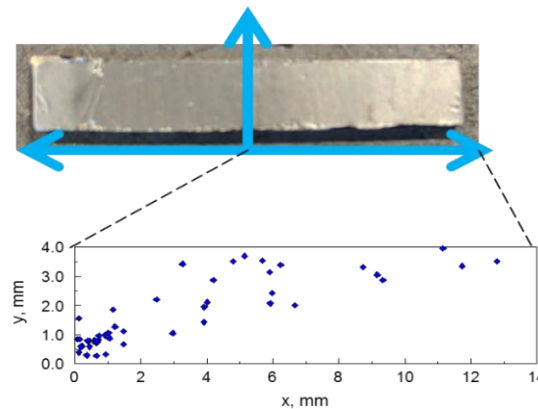
Figure 3.19 A photograph of the foil with quenched particles and a diagram of particle distribution on one side of the foil.
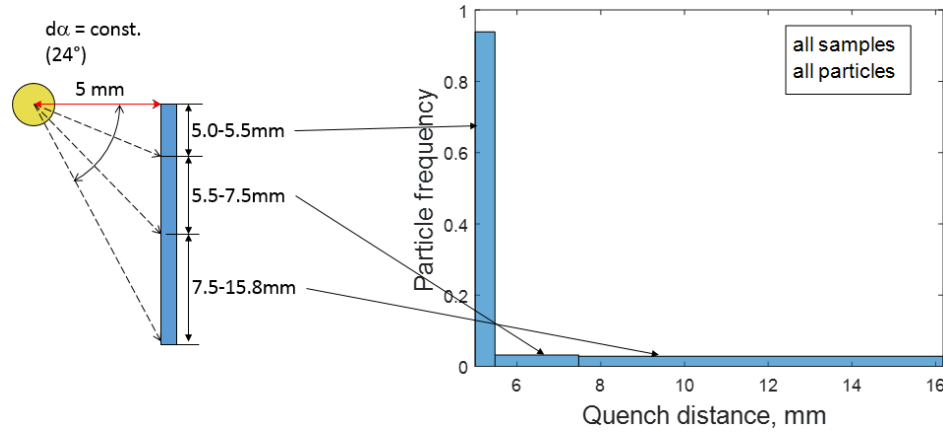
Figure 3.20 Number frequency distribution over quenched distance of captured particles.

The number frequency of captured particles, as shown in **Figure 3.20**, decreased dramatically as the capture distance increased. The quenched particles, as shown in **Figure 3.21**, were classified as two categories of burning, intact and completely burned, two categories of phase-separations, large-scale and small-scale phase-separation, and two categories of structure, spherical and deformed. In **Figure 3.21**, different phases have distinctly different colors with darker color corresponding to the aluminum-rich parts of particles. **Figure 3.21(a)** and **(b)** show the spherical and deformed shape particles containing phases separated on the scale comparable with the dimension of the particles. **Figure 3.21(c)** and **(d)** show the spherical and deformed shape particles with phase-separation occurred on a scale considerably smaller than the dimension of particles. Further, **Figure 3.21(e)** shows intact particles remaining their original shapes and structures. **Table 3.1** listed the total number of quenched particles and percentage of each category captured within different distance ranges. To further illustrate the patterns, the total count of particles with same scales of phase-separations, same kinds of quenched shapes were combined and shown as number fraction of all captured particles in **Table 3.2**. The small-scale phase-separation as the less commonly observed phenomenon indicates that the particles were heated rapidly, possibly originated from the center of combustion and heated directly by

the electro-spark. After a very short duration of heating, those particles were pushed away in the partially molten form by combustion shockwave. The oxidation of aluminum matrix and embedded iron (III) oxide were carried out on the interface and cause the small-scale phase-separation of aluminum oxide and iron. The large-scale separation was observed to be the majority of quenched particles, suggesting that they were surrounding the ignition center, heated by collisions of directly heated particles. The consequential lower heating rate led to evenly melting of particles, and the aluminum oxide and iron collapsed into spherical droplets as a result of surface tension. Thus, the initial nanostructure of the prepared materials was lost. The deformed and spherical shapes were created possibly due to the different temperature to which the particles were heated. This hypothesis was supported by the frequency of those shapes and phase-separation scales.
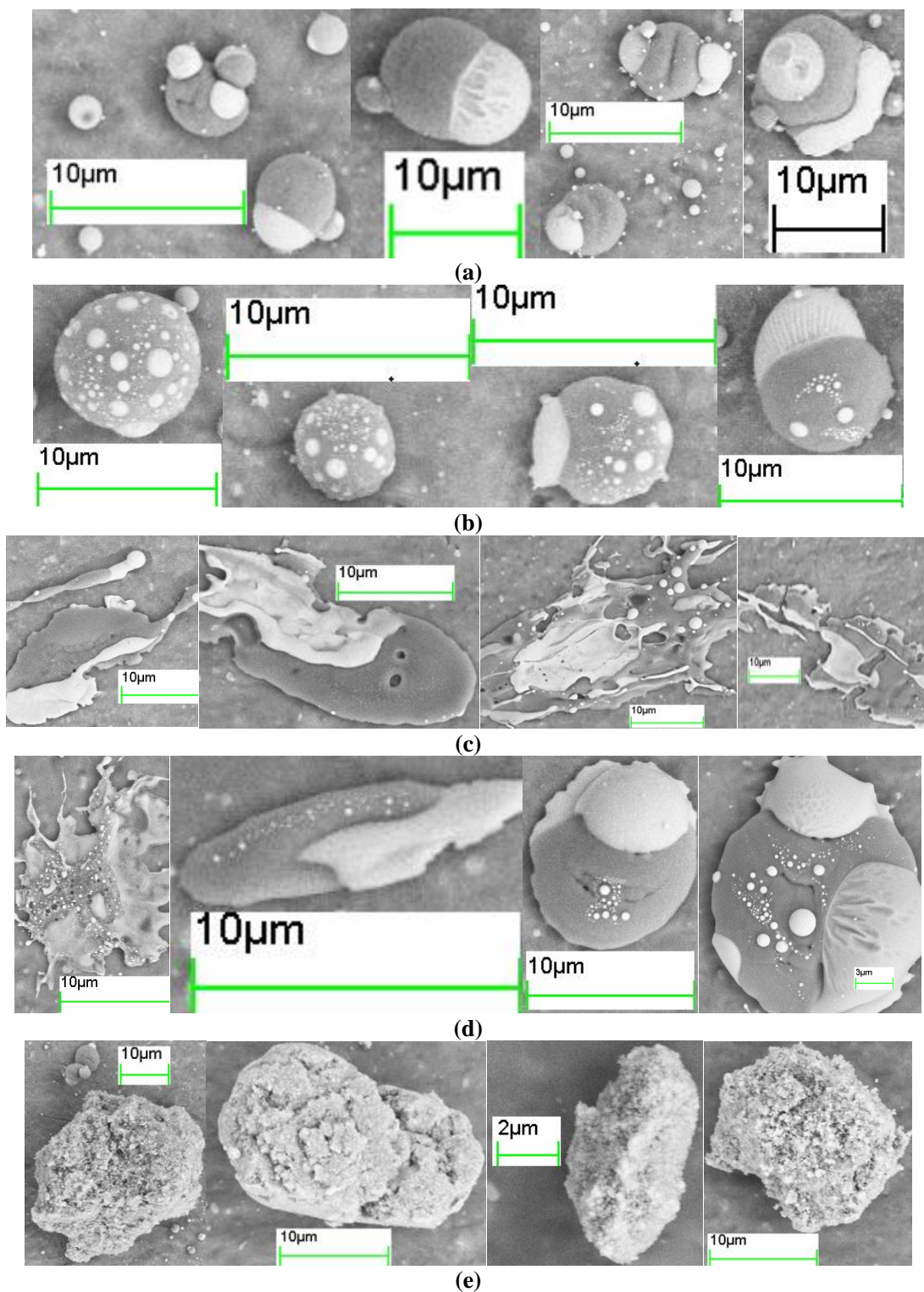
Figure 3.21 Quenched particles with **(a)** large-scale phase-separation and spherical shape; **(b)** small-scale phase-separation and spherical shape; **(c)** large-scale phase-separation and deformed shape; **(d)** small-scale phase-separation and deformed shape; **(e)** intact structure.

Table 3.1 Quenched Particle Structure Classifications and Frequency-Distance Distributions

Sample ID	Distance mm	Particles Number	Large-scale Separation Spherical	Large-scale Separation Deformed	Small-scale Separation Spherical	Small-scale Separation Deformed	Intact
4Al·Fe$_2$O$_3$:Acn	5.0-5.5	59	78%	2%	0%	19%	2%
	5.5-7.5	5	80%	0%	0%	0%	20%
	7.5-15.8	2	0%	50%	0%	0%	50%
4Al·Fe$_2$O$_3$:Dry	5.0-5.5	271	95%	0%	4%	0%	0%
	5.5-7.5	15	67%	7%	0%	27%	0%
	7.5-15.8	5	40%	60%	0%	0%	0%
4Al·Fe$_2$O$_3$:Hex	5.0-5.5	108	76%	17%	4%	4%	0%
	5.5-7.5	1	0%	100%	0%	0%	0%
	7.5-15.8	3	0%	67%	0%	0%	33%
8Al·Fe$_2$O$_3$:Acn	5.0-5.5	169	73%	6%	16%	4%	1%
	5.5-7.5	5	20%	60%	0%	20%	0%
	7.5-15.8	5	20%	40%	20%	20%	0%
8Al·Fe$_2$O$_3$:Dry	5.0-5.5	163	85%	4%	9%	2%	0%
	5.5-7.5	0	0%	0%	0%	0%	0%
	7.5-15.8	8	50%	13%	0%	13%	25%
8Al·Fe$_2$O$_3$:Hex	5.0-5.5	51	47%	25%	8%	18%	2%
	5.5-7.5	3	0%	100%	0%	0%	0%
	7.5-15.8	7	14%	43%	0%	43%	0%

Table 3.2 Frequency of Different Quenched Particle Structures

Samples ID	Number of particles	Phase-Separation Scale Large-scale	Phase-Separation Scale Small-scale	Shape Spherical	Shape Deformed	Intact
4Al·Fe$_2$O$_3$:Acn	66	79%	17%	76%	20%	5%
4Al·Fe$_2$O$_3$:Dry	291	95%	5%	97%	3%	0%
4Al·Fe$_2$O$_3$:Hex	112	92%	7%	77%	22%	1%
8Al·Fe$_2$O$_3$:Acn	179	78%	21%	85%	13%	1%
8Al·Fe$_2$O$_3$:Dry	171	88%	11%	92%	7%	1%
8Al·Fe$_2$O$_3$:Hex	61	72%	26%	48%	51%	2%
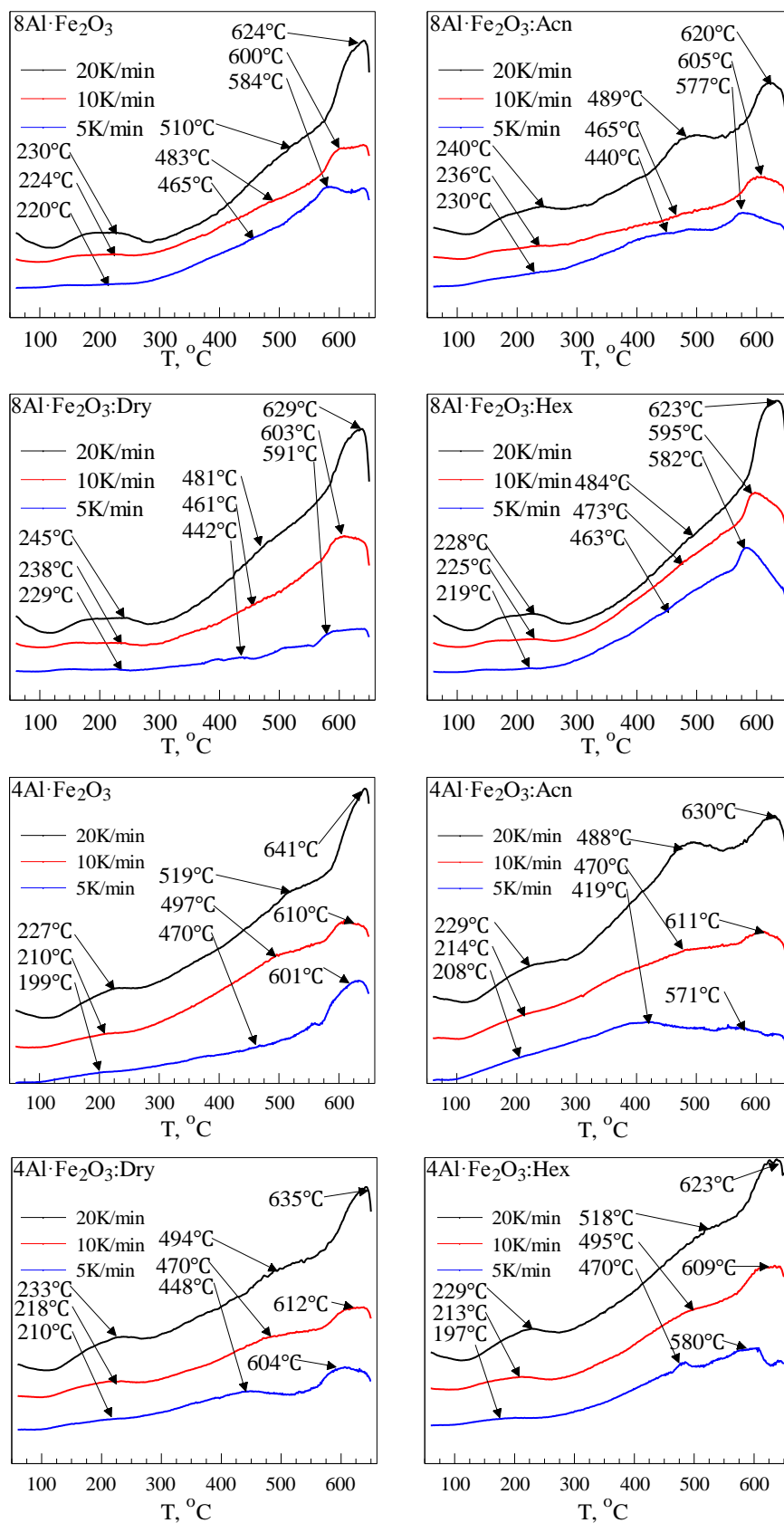
Figure 3.22 DSC for prepared samples heated in pure argon at 5, 10 and 20 K/min.

Finally, results of the thermal kinetic analysis are shown in **Figure 3.22**, the heat flow curves are complicated but showing similar patterns. Although it is not clear in all cases, the DSC curves of all samples exhibited three exothermic peaks at similar temperature ranges, i.e. around 220, 475 and 605 °C. For both $4Al \cdot Fe_2O_3$ and $8Al \cdot Fe_2O_3$ thermites, second step milling with glass beads in all PCAs shows a shift of the second exothermic peak to lower temperature compared to single stage prepared samples. The only exception was the $4Al \cdot Fe_2O_3$ subjected to low-energy milling in hexane. Particularly, the energy release of the second exothermic peak was found to be increased for both $4Al \cdot Fe_2O_3$ and $8Al \cdot Fe_2O_3$ after low-energy milling in acetonitrile.

The activation energy for each exothermic peak was yielded by Kissinger equation [31].:

$$\ln\left(\frac{\beta}{T_{p,i}^2}\right) = \text{Const} - \frac{E_{a,i}}{RT_{p,i}} \tag{3.1}$$

where β is the heating rate:

$$\beta = \frac{\mathrm{d}T}{\mathrm{d}t} \tag{3.2}$$

In equation 3.1, the term on the left-hand side $\ln(\beta/T_{p,i}^2)$ is linearly related to the inverse of peak temperature with $-E_{a,i}/R$ as the slope. The activation Energy of each peak was yielded and shown in **Table 3.3**:

$$E_{a,i} = -\frac{R\,\mathrm{d}\ln\left(\beta/T_{p,i}^2\right)}{\mathrm{d}T_{p,i}^{-1}}$$
$$(3.3)$$

Table 3.3 Activation Energies of DSC Exothermic Peaks for All Prepared Samples

Sample ID	$E_{a,1}$ kJ/mol	$E_{a,2}$ kJ/mol	$E_{a,3}$ kJ/mol
4Al·Fe$_2$O$_3$	**88.0±10.4**	**124.9±10.5**	**195.4±64.9**
4Al·Fe$_2$O$_3$:Acn	117.4±29.8	**68.8±23.9**	**127.4±31.4**
4Al·Fe$_2$O$_3$:Dry	111.1±19.6	**126.2±1.1**	**261.0±75.0**
4Al·Fe$_2$O$_3$:Hex	76.9±1.5	128.2±5.8	181.5±41.8
8Al·Fe$_2$O$_3$	**274.3±31.1**	**134.0±14.6**	**204.7±22.6**
8Al·Fe$_2$O$_3$:Acn	284.8±35.4	**115.5±3.8**	**182.1±36.8**
8Al·Fe$_2$O$_3$:Dry	177.7±15.1	**147.2±0**	**212.5±45.9**
8Al·Fe$_2$O$_3$:Hex	295.8±59.9	293.4±6.0	192.6±41.4

Kissinger equation results showed that low-energy processing in acetonitrile leads to activation energies of the second and the third exothermic peak decreased for both thermites, with the only exception of 4Al·Fe$_2$O$_3$:Hex. On the other hand, the low-energy milling with glass beads in stearic acid appears to increase the activation energy for both 4Al·Fe$_2$O$_3$ and 8Al·Fe$_2$O$_3$. These two observation, only the first one is well co-related with the DSC results, supporting the possibility of chemical alteration brought by low-energy milling in glass beads with acetonitrile.

CHAPTER 4

CONCLUSIONS

The use of glass beads and various process control agents including acetonitrile, hexane and steric acid in the 2nd milling step led to improvement in flowability and combustion performance of nanocomposite thermites, compared to 1 ball-milling step. However, the low-energy $4Al \cdot Fe_2O_3$ processed in acetonitrile and steric acid produced samples with much better flowability than the ones processed in hexane while this phenomenon was not observed in $8Al \cdot Fe_2O_3$ samples. For $4Al \cdot Fe_2O_3$ samples, 2nd milling step in acetonitrile formed more porous agglomeration while this low-energy processing caused de-agglomeration in $8Al \cdot Fe_2O_3$ as finer particles formed, which agreed with observations from SEM. Acetonitrile possibly altered chemistry properties on particle surface due to a significant reduction in ignition temperatures of low-energy processing samples. In ESD experiment, additional low-energy milling did not have an impact on the recorded pressure on $4Al \cdot Fe_2O_3$ samples whereas strong pressure curves and shorter emission traces were observed in $8Al \cdot Fe_2O_3$ samples processing in acetonitrile and steric acid, which indicated that these samples burned better, as a result of better aerosolization, hypothetically. This observation is well-correlated with observations in CVE experiment as they exhibited better combustion behavior than others. Similar observations were seen in $4Al \cdot Fe_2O_3$, but more interestingly, $4Al \cdot Fe_2O_3$ processing in acetonitrile ignited much faster and exhibited strongest combustion behavior than other samples, which also agreed with the ignition test as it had lowest ignition temperature. In quenched particles experiment, a general idea of structure mutation during individual burning particles is proposed and supported by

experimental results. In the kinetic analysis, all low-energy milling samples exhibited similar patterns except for $4Al \cdot Fe_2O_3$:Acn and $8Al \cdot Fe_2O_3$:Acn. DSC result shows that the acetonitrile low-energy milling might alter the thermite structure chemically as indicated by the peak temperature shift and activation energy decrease.

REFERENCES

[1] Son, S. F., Asay, B.W., Busse, J. R., Jorgensen, B. S., Bockmon, B., and Pantoya, M., "Reaction Propagation Physics of Al/MoO$_3$ Nano-composite Thermites." *Twenty-Eighth International Pyrotechnics Seminar, International Pyrotechnics Society*, Fort Collins, CO, 4–9 Nov. 2001, pp. 833–843.

[2] Son, S. F., "Performance and Characterization of Nanoenergetic Materials at Los Alamos." *Material Research Society Symposium Proceedings*, Vol. 800, Materials Research Society, Warrendale, PA, 2004, pp. AA5.2.1–AA5.2.12.

[3] Moore, D. S., Son, S. F., and Asay, B. W., "Time-Resolved Spectral Emission of Deflagrating Nano-Al and Nano-MoO$_3$ Metastable Interstitial Composites." *Propellants, Explosives, Pyrotechnics*, Vol. 29, No. 2, 2004, pp. 106–111.

[4] Granier, J. J., and Pantoya, M. L., "Laser Ignition of Nanocomposite Thermites." *Combustion and Flame*, Vol. 138, No. 4, 2004, pp. 373–383.

[5] Wilson, D. E., and Kim, K., "A Simplified Model for the Combustion of Al=MoO$_3$ Nanocomposite Thermites." *39th AIAA/ASME/SAE/ASEE Joint Propulsion Conference*, Huntsville, AL, AIAA Paper 2003-4536, Hunstville, AL, 2003.

[6] Plantier, K. B., Pantoya, M. L., and Gash, A. E., "Combustion Wave Speeds of Nanocomposite Al=Fe$_2$O$_3$: the Effects of Fe$_2$O$_3$ Particle Synthesis Technique." *Combustion and Flame*, Vol. 140, No. 4, 2005, pp. 299–309.

[7] Gash, A. E., Tillotson, T. M., Satcher, J. H., Hrubesh L. W., Jr., and Simpson. R. L., "New Sol-Gel Synthetic Route to Transition and MainGroup Metal Oxide Aerogels Using Inorganic Salt Precursors." *Journal of Non-Crystalline Solids*, Vol. 285, Nos. 1–3, 2001, pp. 22–28.

[8] Subramaniam, S., Hasan, S., Bhattacharya, S., Gao, Y., Apperson, S., Hossain, M., Shende, R. V., Gangopadhyay, S., Redner, P., Kapoor, D., and Nicolich, S., "Self-Assembled Nanoenergetic Composite." *Material Research Society Symposium Proceedings*, Vol. 896, Materials Research Society, Warrendale, PA, 2006, pp. H01-05.1–05.6.

[9] Blobaum, K. J., Reiss, M. E., Plitzko, Lawrence, J. M., and Weihs, T. P., "Deposition and Characterization of a Self-Propagating CuO$_x$/Al Thermite Reaction in a Multilayer Foil Geometry." *Journal of Applied Physics*, Vol. 94, No. 5, 2003, pp. 2915–2922.

[10] Blobaum, K. J., Wagner, A. J., Plitzko, J. M., Van Heerden, D., Fairbrother, D. H., and Weihs, T. P., "Investigating the Reaction Path and Growth Kinetics in CuO_x=Al Multilayer Foils." *Journal of Applied Physics*, Vol. 94, No. 5, 2003, pp. 2923–2928.

[11] Wang, J., Besnoin, E., Duckham, A., Spey, S. J., Reiss, M. E., Knio, O.M., and Weihs, T. P., "Joining of Stainless-Steel Specimens with Nanostructured Al-Ni Foils." *Journal of Applied Physics*, Vol. 95, No. 1, 2004, pp. 248–256.

[12] Schoenitz, M., Ward, T., and Dreizin, E. L., "Fully Dense Nanocomposite Energetic Powders Prepared by Arrested Reactive Milling." *Material Research Society Symposium Proceedings*, Vol. 800, Materials Research Society, Warrendale, PA, 2004, pp. AA2.6.1–AA2.6.6.

[13] Schoenitz, M., and Dreizin, E. L., "Nano-Composite Energetic Powders Prepared by Arrested Reactive Milling." *U.S. Patent Application No. 10/988,183*, filed 12 Nov. 2004.

[14] Zhang, F., Gauthier, M., and Cojocaru, C., "Sub-fragmentation of structural reactive material casings under explosion." *AIP Conference Proceedings*, Vol. 1793, No. 1, AIP Publishing, 2017.

[15] Umbrajkar, S. M., Zhu, X., Schoenitz, M., and Dreizin, E. L., "Effect of Compositional and Structural Refinement on the Ignition and Combustion of Reactive Nanocomposite Powders." *Fourth Joint Meeting of the U.S. Sections of the Combustion Institute*, Combustion Inst., Pittsburgh, PA, 2005, pp. D37/1–D37/6.

[16] Umbrajkar, S. M., Schoenitz, M., and Dreizin, E. L., "Control of Structural Refinement and Composition in Al–MoO_3 Nanocomposites Prepared by Arrested Reactive Milling." *Propellants, Explosives, Pyrotechnics*, Vol. 31, No. 5, 2006, pp. 382–389.

[17] Butscher, A., Bohner, M., Hofmann, S., Gauckler, L., and Müller, R., "Structural and material approaches to bone tissue engineering in powder-based three-dimensional printing." *Acta biomaterialia*, Vol. 7, No. 3, 2011, pp. 907-920.

[18] Dreizin, E. L., "Metal-based reactive nanomaterials." *Progress in Energy and Combustion Science*, Vol. 35, No. 2, 2009, 141-167.

[19] Umbrajkar, S. M., Schoenitz, M., and Dreizin, E. L., "Exothermic Reactions in Al–CuO Nanocomposites." *Thermochimica Acta*, Vol. 451, Nos. 1–2, 2006, pp. 34–43.

[20] Schoenitz, M., Umbrajkar, S., and Dreizin, E. L., "Kinetic Analysis of Thermite Reactions in Al–MoO_3 Nanocomposites." *Journal of Propulsion and Power*, Vol. 23, No. 4, 2007, pp. 683–687.

[21] Son, S. F., "Performance and Characterization of Nanoenergetic Materials at Los Alamos." *Material Research Society Symposium Proceedings*, Vol. 800, Materials Research Society, Warrendale, PA, 2004, pp. AA5.2.1–AA5.2.12.

[22] Prentice, D., Pantoya, M. L., and Clapsaddle. B. J., "Effect of Nanocomposite Synthesis on the Combustion Performance of a Ternary Thermite." *Journal of Physical Chemistry B*, Vol. 109, No. 43, 2005, pp. 20180–20185.

[23] Subramaniam, S., Hasan, S., Bhattacharya, S., Gao, Y., Apperson, S., Hossain, M., Shende, R. V., Gangopadhyay, S., Redner, P., Kapoor, D., and Nicolich, S., "Self-Assembled Nanoenergetic Composite." *Material Research Society Symposium Proceedings*, Vol. 896, Materials Research Society, Warrendale, PA, 2006, pp. H01-05.1– 05.6.

[24] Blobaum, K. J., Reiss, M. E., Plitzko, Lawrence, J. M., and Weihs, T. P., "Deposition and Characterization of a Self-Propagating CuOx/Al Thermite Reaction in a Multilayer Foil Geometry." *Journal of Applied Physics*, Vol. 94, No. 5, 2003, pp. 2915–2922.

[25] Ward, T. S., Trunov, M. A., Schoenitz, M., & Dreizin, E. L., "Experimental methodology and heat transfer model for identification of ignition kinetics of powdered fuels." *International Journal of Heat and Mass Transfer*, Vol. 49, No. 25, 2006, pp. 4943-4954.

[26] Williams, R. A., Patel, J. V., & Dreizin, E. L., "Ignition of fully dense nanocomposite thermite powders by an electric spark." *Journal of Propulsion and Power*, Vol. 30, No. 3, 2014, pp. 765-774.

[27] Eapen, B. Z., Hoffmann, V. K., Schoenitz, M., & Dreizin, E. L., "Combustion of aerosolized spherical aluminum powders and flakes in air." *Combustion Science and Technology*, Vol. 176, No. 7, 2004, pp. 1055-1069.

[28] Santhanam, P.R., Hoffmann, V.K., Trunov, M.A. and Dreizin, E.L., "Characteristics of aluminum combustion obtained from constant-volume explosion experiments." *Combustion Science and Technology*, Vol. 182, No. 7, 2010, pp. 904-921.

[29] Schoenitz, M., Dreizin, E.L. and Shtessel, E., "Constant volume explosions of aerosols of metallic mechanical alloys and powder blends." *Journal of propulsion and power*, Vol. 19, No. 3, 2003, pp. 405-412.

[30] Monk, I., Williams, R.A., Xinhang, L., Dreizin, E.L., "Electro-static discharge ignition of monolayers of nanocomposite thermite powders prepared by arrested reactive milling." *Combustion Science and Technology*, Vol. 182, No. 8, 2015, pp.1276-1294.

[31] Vyazovkin, S., Burnham, A.K., Criado, J.M., Pérez-Maqueda, L.A., Popescu, C., Sbirrazzuoli, N. "ICTAC Kinetics Committee recommendations for performing kinetic computations on thermal analysis data." *Thermochimica Acta*, Vol. 520, No. 1, 2011, pp.1-19.